Quiescence-inducing 3D-engineered matrix uncovers mechanosensitive and drug protective FHL2-p21 signaling axis

Sadra Bakhshandeh[1], Hubert M. Taïeb[1], Adithi R. Varadarajan[2], Susanna M. Lissek[3], Sarah M. Hücker[2], Xin Lu[2], Daniela S. Garske[1], Sarah A. E. Young[1], Jörg Contzen[4, 5, 6], Manfred Gossen[5, 6], Stefan Kirsch[2], Jens Warfsmann[2], Kamran Honarnejad[2], Christoph A. Klein[2, 3], Amaia Cipitria[1, 7, 8]*

[1]Department of Biomaterials, Max Planck Institute of Colloids and Interfaces, Potsdam, Germany

[2]Division of Personalized Tumor Therapy, Fraunhofer Institute for Toxicology and Experimental Medicine, Regensburg, Germany

[3]Experimental Medicine and Therapy Research, University of Regensburg, Regensburg, Germany

[4]Department of Experimental Neurology, Charité - Universitätsmedizin Berlin, Berlin, Germany

[5]Institute of Active Polymers, Helmholtz-Zentrum Hereon, Teltow, Germany

[6]Berlin-Brandenburg Center for Regenerative Therapies, Charité Campus Virchow Klinikum, Berlin, Germany

[7] Group of Bioengineering in Regeneration and Cancer, Biodonostia Health Research Institute, San Sebastian, Spain

[8]IKERBASQUE, Basque Foundation for Science, Bilbao, Spain

Correspondence to: amaia.cipitria@mpikg.mpg.de

Abstract

Resected tumors frequently relapse with distant metastasis, despite systemic treatment. Cellular quiescence has been identified as an important mechanism underlying such drug resistance enabling late relapse. Nonetheless, hurdles associated with detection and isolation of disseminated cancer cells (DCCs) in disease-free patients urge the need for *in vitro* models of quiescent cells suited for drug screening campaigns. Here, we explore a quiescence-inducing 3D-engineered matrix based on ultraviolet light-initiated thiol-ene-crosslinked alginate hydrogels, which generate mechanical confinement and induce growth arrest and survival against chemotherapy in cancer cells. As underlying mechanism, we identified stiffness-dependent nuclear localization of the four-and-a-half LIM domains 2 (FHL2) protein, leading to p53-independent high p21$^{Cip1/Waf1}$ nuclear expression, validated in murine and human tissue. Suggestive of a resistance-causing role, cells in the quiescence-inducing matrix became sensitive against chemotherapy upon FHL2 downregulation. Thus, our biomaterial-based approach will enable systematic screens for novel compounds suited to eradicate potentially relapsing, dormant cancer cells.

Introduction

Most cancer-associated deaths are due to metastasis, with eventual relapses spanning from years to decades despite adjuvant and chemotherapies(*1, 2*). Cancer dormancy has been described as one of the main mechanisms of evasion, which, due to its asymptomatic nature, poses significant technical and ethical challenges for the identification, isolation and investigation of DCCs(*3*). This calls for reliable *in vitro* culture systems to mimic this geno/phenotypic state to finally enable scalable drug screening campaigns for the identification of promising target drugs. Material-based, bioengineered-niche approaches have been previously pursued to induce and/or preserve the quiescence of astrocytes(*4*) and muscle stem cells(*5*), maintain neural progenitor(*6*) and hematopoietic cell stemness(*7*), investigate mechanical memory(*8*) and differentiation of stem cells(*9*), as well as to investigate cancer cell cycle progression(*10, 11*). Here, we harnessed a similar approach by developing ultraviolet (UV) light-initiated, thiol-ene-mediated, covalently-crosslinked alginate hydrogels, which through 3D mechanical confinement induce and maintain large populations of single breast cancer cells in a growth-arrested state. We showed that artificial quiescence-inducing matrices select for distinct populations of growth-arrested cells, with cells in the G_0/G_1 cell cycle phase being more resistant to confinement. Combined with RNA sequencing, we revealed a stiffness-dependent nuclear localization of the four-and-a-half LIM domains 2 (FHL2) protein as an underlying mechanism of quiescence, leading to a p53-independent high $p21^{Cip1/Waf1}$ nuclear expression, validated in murine and human tissue. Suggestive of a growth arrest-mediated drug resistance, quiescent cells became sensitive against drug treatment upon FHL2 downregulation. This biomaterial-based approach with mechanically-induced quiescent cancer cells offers therapeutic applications as a simple and scalable method, to investigate large populations of dormant cancer cells, otherwise rare and inaccessible in large numbers from clinical settings, and for high throughput drug screens of novel compounds to eradicate potentially relapsing DCCs.

Results

3D mechanical confinement via covalently-crosslinked alginate yields distinct fractions and populations of growth-arrested cells based on hydrogel composition

Building on the now widely acknowledged role of the ECM in cancer induction and progression(*12, 13*), we employed a versatile ECM-mimicking hydrogel encapsulation approach to investigate the effect of ECM-mediated 3D mechanical confinement on cell cycle progression. We used ultraviolet (UV) light-initiated thiol-ene-crosslinked alginate(*14*), an inherently inert hydrogel (non-cell adherent and non-degradable) which allows for selective modulation of parameters such as stiffness, cell adhesion or degradation (Fig.1a). Cells were encapsulated in the presence (or absence) of adhesion ligands (RGD), within degradable matrix metalloproteinases (MMP)-sensitive or non-degradable dithiothreitol (DTT)-crosslinked hydrogels (Fig.1a and Supp.Fig.1). The stiffness of the hydrogels ranged between 0.5-13kPa as a function of crosslinker concentration (Fig.1b). To monitor cell cycle progression in real-time, we genetically modified widely-used triple-negative MDA-MB-231 (MDA231) and luminal MCF7 breast cancer cell (BCC) lines, known to disseminate to secondary organs in *in vivo* models, with the fluorescence-ubiquitination-based cell cycle indicator 2 (FUCCI2)(*15, 16*) (Fig.1c). Time-lapse imaging of MDA-FUCCI2 cells encapsulated within alginate hydrogels of different stiffness (soft for 1kPa and stiff for 10kPa), adhesion and degradation properties, as well as on two-dimensional tissue culture plastic (2D-TCP) and in 3D Matrigel, was performed over a period of 4-5 days, followed by quantification of the cell cycle state at the experimental endpoint (Fig.1d, Supp.Mov.1). 3D Matrigel and 2D TCP yielded highly proliferative (Ki67+) and metabolically active cells (resazurin reduction) in the form of 3D spheroids and single cells, respectively (Fig.1d, Supp.Fig.2b,d). Cells within the 3D alginate groups remained mostly as single cells, with the highest fraction of $S/G_2/M$ phase cells being in the soft

95 group, while the stiff adherent (RGD) and degradable (MMP-sensitive) groups displayed a lower
96 percentage of S/G$_2$/M and higher fraction of G$_0$/G$_1$ phase cells (Fig.1d). 3D alginate stiff yielded
97 the highest fraction of cell cycle-arrested cells over 5 days (Fig.1d), while preserving high viability
98 (Supp.Fig.2a). Interestingly, we noticed different sub-populations of cell cycle-arrested cells as a
99 function of the expression (or lack of) of the licensing factor cdt1 (G$_0$/G$_1$ cdt1+/–; Fig.1d, Fig.2a,
100 Supp.Mov.2-7). A recent mapping of protein dynamics during cell cycle progression revealed that
101 the expression patterns of cdt1 is highly dynamic and distinctive of different levels of quiescence,
102 with the lowest (cdt1-) identifying a longer time spent in a growth-arrested state(*17*). MDA231 cells
103 in quiescence-inducing alginate stiff hydrogels displayed higher resistance to chemotherapy
104 compared to cells in proliferation-permissive 3D Matrigel (Supp.Fig.2e) and, reminiscent of post-
105 therapeutic relapses in clinical settings, were able to exit the growth-arrested state and resumed
106 proliferation when retrieved from the hydrogels and seeded on 2D TCP (Supp.Fig.2c).

Dynamics of cell cycle and viability correlation reveal that G$_0$/G$_1$ cells are substantially more resistant to 3D mechanical confinement than cells in the S/G$_2$/M phase

109 To understand the dynamics of 3D mechanical confinement-induced growth arrest, we
110 tracked single-cell MDA-FUCCI2 fluorescence intensity (f.i.) within stiff hydrogels. Cells which
111 were in the G$_0$/G$_1$ state at the time of encapsulation, had either lost (cdt1-) (Fig.2a1, b) or kept
112 (cdt1+) (Fig.2a2, b) their fluorescence by the end of the experiment. On the other hand, in almost
113 every cell initially in the S/G$_2$/M phase, we observed a decrease in f.i. within the first few hours
114 after encapsulation (Fig.2a3, b). By correlating cell's FUCCI2 imaging and *in situ* viability staining
115 (calcein+; Fig.2c), we revealed that the vast majority of viable cells at day 5 were initially in the
116 G$_0$/G$_1$ cycle state (Fig.2c, d). We validated these results for MCF7-FUCCI2 cells (Fig.2d),
117 confirming that cells in the G$_0$/G$_1$ state are more resilient to 3D mechanical confinement compared
118 to cells in the S/G$_2$/M phase.

Gene expression analysis of cells in quiescence-inducing versus proliferation-permissive 3D matrices

121 We then looked into the gene expression of quiescence-induced cells in more details. RNA-
122 sequencing on live cells retrieved from 3D alginate stiff (Fig.3a) revealed enrichment of cell cycle
123 and retinoblastoma-associated molecular pathways (Fig.3b-d, Supp.Fig.3, 4), as well as regulation
124 of senescence, autophagy and apoptosis processes when compared to cells retrieved from 3D
125 Matrigel. In particular, we noticed strong enrichment of inflammatory response-associated
126 pathways (TNF, NFkB and IL-17 signaling) and DNA damage stimuli response (ATM, p53 and
127 miRNA regulation of DNA damage) (Fig.3b-e, Supp.Fig.3, 4). Intriguingly, we noticed that despite
128 increased mRNA expression of *cdkn1a* (coding for the p21 protein) upon culture in 3D alginate
129 stiff compared to 3D Matrigel, the levels of its key upstream cell cycle regulator *p53* is lower
130 (Fig.3e), hinting to a potential p53-independent mechanism regulating p21 expression(*18*). This
131 matches the lack of correlation of p53-p21 observed in patients with estrogen receptor negative
132 (ER-) breast cancer (Supp.Fig.5). Noticing the particularly high levels of p21 (*cdkn1a*) expression
133 among other genes in 3D alginate (Fig.3e) and its relevance in cell cycle regulation, we decided to
134 investigate the role of p21 in regulating mechanically-induced cancer cell cycle arrest in more
135 detail.

p21 and FHL2 localization in 3D matrices is stiffness-dependent and FHL2 mediates p21 localization and Ki67 expression

138 Despite the now widely acknowledge advantages of 3D vs. 2D culture systems in studying
139 physiologically-relevant cellular processes(*19*), the role of dimensionality in the expression,
140 localization and function of p21 remains underexplored. This is of utmost importance considering
141 that in cancer cells the p21 oncogenic vs. suppressing function is known to depend on its level of
142 expression and intracellular localization(*18*). We therefore assessed these features across different

143 3D culture systems, focusing on soft and stiff 3D alginate hydrogels. As expected, the fraction of
144 p21-positive cells was significantly higher in 3D alginate stiff compared to soft or 3D Matrigel
145 (Supp.Fig.6), accompanied by strong enrichment of DNA repair-associated pathways (Fig.4a-b and
146 Supp.Fig.7). Importantly, cells in 3D alginate stiff revealed a significantly higher nuclear vs.
147 cytoplasmic (nuc./cyto. ratio) localization of p21 compared to the soft group, together with a lower
148 fraction of proliferative cells (Ki67 expression) (Fig.4c). Inhibiting MEK/ERK, PI3K/Akt and JNK,
149 as some of the major signaling pathways regulating cell proliferation, displayed a strong effect on
150 p21 localization (Fig.4d).

151 Previous work on 2D cultures had found that, in MDA231 cells, p21 is induced in response
152 to treatment with DNA damaging drugs such as doxorubicin, and this is mediated by FHL2 in a
153 p53-independent manner[20]. Notably, FHL2 was shown to be stably expressed in only a small
154 subset of BCC lines with MDA231 being among the highest[20]. Nonetheless, FHL2 localization
155 and functional role in physiologically-relevant 3D cultures had not been addressed. We therefore
156 investigated the nuc./cyto. ratio of FHL2 in 3D stiff compared to soft alginate hydrogels.
157 Surprisingly, and in stark contrast to 2D cultures where soft 2D substrates lead to nuclear
158 accumulation of FHL2[21], we observed a significantly higher expression and nuc./cyto. ratio of
159 FHL2 in 3D stiff compared to soft alginate hydrogels (Fig.4e). This effect was mitigated by
160 inhibiting MEK/ERK and PI3K/Akt pathways but not JNK (Fig.4f). Importantly, knock-down of
161 FHL2 revealed a decrease in p21 nuclear localization in 3D stiff hydrogels (Fig.4g), as well as an
162 increase in proliferation activity (Ki67; Fig.4f), pointing to FHL2 being upstream of p21. The
163 correlated expression of *cdkn1a* and *FHL2* is also found in tumor samples of patients with ER-
164 breast cancer (Supp.Fig.8).

165 FHL2 knockdown sensitizes cells to chemotherapy

166 We then investigated whether FHL2 knockdown sensitizes cells to chemotherapy. FHL2-
167 silenced cells in 3D alginate stiff displayed higher viability and metabolic activity than wild-type
168 MDA231 when untreated (vehicle) (Fig.5a). Upon exposure to mitosis-blocking chemotherapeutic
169 Paclitaxel in a concentration-dependent fashion (0.01-0.5mM), a significant reduction in viability
170 and metabolic activity was observed (Fig.5a), pointing to a chemo-sensitizing effect upon FHL2
171 knockdown.

172 FHL2 expression and localization in murine tissue, human primary breast tumor and human
173 early DCCs

174 Finally, to assess the implications for human disease, we investigated FHL2 expression and
175 localization in a preclinical mouse model with metastatic breast cancer and in human primary tumor
176 biopsies. Remarkably, single quiescent MDA231 cells (bone-tropic 1833 subclone) spontaneously
177 disseminated to the mouse femur revealed nuclear FHL2, as opposed to proliferative clusters with
178 cytoplasmic FHL2 (Fig.5b, Supp.Fig.9). Similarly, human tissue biopsies of breast tumor reveal a
179 primarily cytoplasmic/membranous localization of FHL2 (Fig.5c), matching our observation in 3D
180 Matrigel (Fig.5d). Furthermore, we investigated human early DCCs of an M0 breast cancer patient,
181 with only microscopy evidence of metastasis and no clinical or radiographic evidence of distant
182 metastasis. Disseminated breast cancer cells (cytokeratin+, an epithelial marker) in the sentinel
183 lymph node displayed varying FHL2 signal intensity suggestive of functional heterogeneity (Fig.5e,
184 f).

185 To sum up, ligand-rich, proliferation-permissive microenvironments maintain FHL2 in the
186 membranous regions, whereas in low or non-adherent microenvironments the increase in
187 mechanical confinement (stiffness) results in FHL2 translocation to the nucleus, leading to high
188 p21 nuclear expression, cell cycle arrest and chemo-resistance (Fig.6).

189
190

Discussion

191

192   In this study, we use a 3D quiescence-inducing engineered matrix to investigate a
193   mechanism of chemoresistance in mechanically-induced dormant BCCs. Systematic tuning of three
194   variables (adhesion via RGD, degradability through MMP-sensitive crosslinkers and stiffness)
195   enables generation of different fractions of cell populations with defined and controllable cell cycle
196   status. Here, we harness this approach and reveal a stiffness-dependent nuclear localization of the
197   FHL2 protein which leads to p53-independent nuclear expression of p21 as a quiescence and
198   resistance-conferring mechanism. We further show that the expression and localization of both p21
199   and FHL2 in 3D to be strikingly different than previously-reported 2D studies, where FHL2
200   shuttling to the nucleus was shown to be substrate rigidity-dependent, such that on soft surfaces (as
201   opposed to stiff substrates where mechanical tension is higher) it would translocate to the nucleus
202   and induce p21 expression(21). In contrast, in 3D matrices ligand-rich environments such as in
203   basement membrane matrices or primary breast tumor sites, FHL2 accumulates in adhesion
204   sites(21), whereas loss of adhesion (occurring in intrinsically non-adherent materials such as
205   alginate), results in FHL2 release from sub-membranous regions and shuttling to cytoplasmic (soft
206   alginate) and nuclear (stiff alginate) regions. This cascade leads to p21 nuclear expression, cell
207   cycle arrest and drug resistance for the latter (Fig.5e). Such dimensionality-dependent behavior has
208   been similarly reported for YAP mechanotransduction in the context of breast tumor
209   progression(22) and stem cell fate(23). Thus, it is critical to take into account the context-dependent
210   role of the FHL2-p21 signaling axis, given its potential dual oncogenic vs. suppressive function(18,
211   24). Notably, omission of adhesion ligands in our quiescence-inducing matrix was intentional,
212   stemming from recent *in vivo* observations(25) where single DCCs were shown to reside in a
213   dormant state with expressed but not engaged integrin receptors. Other studies have similarly
214   observed DCCs expressing low levels of adhesion molecules(26), and integrin activation being a
215   central mediator leading to their awakening(26–29).

216   FHL2 has been previously shown to concentrate at RNA polymerase (Pol) II sites(21),
217   inducing c-Jun, IL6 and IL8 transcription. This is reflected in our sequencing data by the strong
218   enrichment of RNA Pol II associated genes, with JUN, IL6 and IL8 being among the top ten (out
219   of 9427) differentially regulated genes in the alginate stiff group (Fig.3b-e). This is in line with a
220   recent study showing IL6 pathway activation in patient-derived early disseminated BCC in bone
221   marrow(30).

222   To further support our findings, we investigated breast cancer cells disseminated to the bone
223   in a metastasis mouse model, human tissue biopsies of primary breast cancer and early DCCs of an
224   M0 breast cancer patient. Here we noted nuclear FHL2 localization in single dormant DCCs
225   (Fig.5b) as opposed to cytoplasmic FHL2 corresponding to high proliferation activity (Ki67+) in a
226   mouse model of breast cancer metastasis (Fig 5b). Likewise, cytoplasmic/membranous FHL2 is
227   observed in human primary breast tumor biopsies (Fig.5c) matching the findings of proliferating
228   cancer cells in 3D Matrigel (Fig. 5d). This is in agreement with screenings of normal and malignant
229   human breast tissues revealing higher FHL2 expression for the latter, as shown in previous
230   studies(20, 31) and UALCAN database, while high FHL2 expression in ER- patients is associated
231   with lower relapse-free survival rate (Supp.Fig.10). A number of disseminated breast cancer cells
232   (cytokeratin+) were found in the sentinel lymph node both as single cells (Fig. 5e) and within cell
233   clusters (Fig. 5f). We noted a substantial heterogeneity among the DCCs, further supporting the
234   notion that various phenotypes exist in patients that may require different targeting approaches.

235   To conclude, we identify a stiffness-mediated FHL2 signaling mechanism in 3D
236   bioengineered matrices inducing breast cancer cell quiescence and drug resistance, which
237   recapitulates several aspects of patient-derived DCCs and mouse models of metastasis. Further, this
238   approach can be exploited to generate large populations of single growth-arrested cells for simple,

239 fast and potentially scalable drug screening, since these are known to be rare and inaccessible in
240 large numbers from clinical settings.

241

Materials and Methods

Synthesis of peptide-crosslinked alginate hydrogels

244   Norbornene-modified alginate hydrogels with thiol-ene crosslinking were synthesized as
245 previously described(*32*). Briefly, high molecular weight (265 kDa; HMW), high guluronic acid,
246 sodium alginate (Pronova MVG; NovaMatrix) was dissolved at 1% w/v in 0.1 M 2-
247 (N- morpholino)ethanesulfonic acid (MES; Sigma-Aldrich), 0.3M NaCl (EMD Millipore) buffer
248 (pH 6.5) overnight at room temperature. N-hydro-xysuccinimide (NHS; Sigma-Aldrich), followed
249 by 1-ethyl-3-(3-dimethylami-nopropyl)-carbodiimide hydrochloride (EDC; Sigma-Aldrich) were
250 added drop-wise at 5000 molar equivalents to the alginate solution while stirring. To functionalize
251 the alginate backbone with norbornene functional groups, 5-norbornene-2-methylamine (TCI
252 Deutschland GmbH) was added at a theoretical degree of substitution (DStheo) of 300 molecules
253 per alginate chain. The final concentration of both reactions was 0.6% w/v and was run while
254 stirring at 700 rpm at room temperature for 20 h. Next, the solution was quenched by adding
255 hydroxylamine (Sigma-Aldrich), followed by dialysis (Spectra/Por 6, MWCO 3.5 kDa; Spectrum)
256 against a salt gradient (6 g/L to 0 g/L; Sigma-Aldrich) in ddH_2O for 3 days with 3-4 changes per
257 day. The solution was then purified with activated charcoal (Sigma-Aldrich), sterile-filtered (0.22
258 μm; Steriflip-GP; Merck) and lyophilized. To assess the actual degree of substitution, NMR
259 measurements were performed using an Agilent 600 MHz PremiumCOMPACT equipped with
260 Agilent OneNMR Probe (256 scans), with samples dissolved at a final concentration of 1.5% w/v
261 in deuterium oxide (D_2O) (Supp. Fig 1b, c).

Casting of peptide-crosslinked alginate hydrogels

263   For hydrogel casting, the VPMS↓MRGG sequence was chosen as the enzymatically-
264 degradable peptide crosslinker (↓ denotes the MMP cleavage site), ordered from WatsonBio
265 Sciences at 98% purity with trifluoroacetic acid removal (Supp. Fig 1d). Double-cysteine
266 containing dithiothreitol (DTT, Sigma-Aldrich, 43816) was used as the non-degradable crosslinker.
267 Before casting, norbornene-modified alginate and the photoinitiator (Irgacure 2959; Sigma-
268 Aldrich) were dissolved in phosphate-buffered saline (PBS) overnight at 50 °C under shaking.
269 Alginate and photoinitiator concentrations were kept at 2 and 0.5% w/v respectively. The
270 concentration of the crosslinker was changed to yield hydrogels with different mechanical
271 properties. After mixing, the solution was pipetted with positive-displacement pipettes on a glass
272 plated and covered with a dichloromethylsilane-coated glass slide (≥99.5%; Sigma-Aldrich). To
273 initiate thiol-ene crosslinking, the mixture was exposed to UV light (365 nm at 10 mW/cm^2,
274 OmniCure S2000) by placing the gel sheet in a custom-built curing chamber for 10 min. Gels were
275 then punched out using biopsy punches of 4-6 mm (Integra Miltex) and washed with PBS until
276 further use. To render norbornene-modified alginate adherent, a thiol-containing RGD sequence
277 (CGG- GGRGDSP; Peptide 2.0) was added to the gel precursor mix (at 0.95 mM) to bind residual
278 norbornene groups via UV-mediated thiol-ene chemistry. For 3D cell encapsulation, a cell
279 suspension ($5x10^5$ cells/ mL) was added to the precursor solution and mixed before UV exposure.
280 Matrigel (356237, Corning) was used at 100% w/v concentration (~ 10mg/mL).

Mechanical characterization

282   Rheology measurements were performed to calculate the elastic modulus (E) of pre-formed
283 gels. Norbornene-modified alginate (2% w/v) hydrogels with different stiffness were cast by
284 changing the DTT crosslinker concentration (0.01-1 mg/mL). After gel equilibration overnight in
285 PBS, frequency sweep measurements were performed from 0.01 to 10 Hz at 1% shear strain with
286 an 8 mm parallel plate (PP08, Anton Paar) using a rheometer (Physica MCR 301; Anton Paar),

287 while keeping the temperature at 25 °C with a Peltier cooling module. The initial E modulus was
288 then calculated as follows: $E = 2G(1 + \vartheta)$ and $G = \sqrt{G'^2 + G''^2}$ where G, G' and G'' are the shear,
289 storage and loss moduli, respectively, and ϑ the Poisson's ratio with a value of 0.5 for
290 hydrogels(33).

Cell culture

292 MDA-MB-231 (HTB-26; ATCC), MDA-MB-231-1883 BoM (provided by Dr. Joan
293 Massagué and purchased from the Antibody and Bioresource Core Facility of the Memorial Sloan
294 Kettering Cancer Center, USA. The subclone 1833 is a bone tropic human cell line deriving from
295 a metastasis formed by MDA-MB-231 TGL cells hosted in a mouse(34, 35),which in turn are
296 MDA-MB-231 (HTB-26; ATCC) human epithelial breast cancer cells stably transduced with a
297 lentivirus expressing a triple-fusion reporter(36)) and MCF-7 (HTB-22; ATCC) human breast
298 cancer cell lines were cultured in low glucose Dulbecco's Modified Eagle's Medium (D6046;
299 Sigma-Aldrich) with 10% v/v fetal bovine serum (S0615, Sigma-Aldrich) and 1%
300 penicillin/streptomycin (Gibco). For MCF-7 cells, 0.1% insulin (I1882, Sigma-Aldrich) was added.
301 Cells were then incubated in a 5% CO_2 environment at 37 °C and passaged every 3-5 days.

Viability and metabolic activity characterization

303 Live and dead cells were stained with 1.6 mM calcein AM (C125400; TRC) and 4 mM
304 ethidium homodimer-1 (EthD-1 L3224; ThermoFisher), respectively. To measure metabolic
305 activity, Presto blue (ThermoFisher) was used. Briefly, after 1 and 7 days of incubation, cell culture
306 medium was replaced with 10% Presto blue reagent in DMEM and the plate incubated for at least
307 4 h at 37 °C. Next, 100 µL of the supernatant was transferred to a black 96 well plate (655892,
308 Greiner Bio-one) and fluorescence emission was measured at 590 nm (Cytation5, BioTek). ATP
309 concentration was measured using CellTiter-Glo (Promega) according to the manufacturer's
310 instruction. Briefly, a 1:1 volume of reagent and culture medium was added to each sample of a
311 black 96 well plate (655892, Greiner Bio-one), shaken for 10 min at room temperature, and allowed
312 to equilibrate for another 20 min before measuring bioluminescence signal (Cytation5, BioTek).

Lentiviral particle production, transduction and generation of FUCCI2 breast cancer cell lines

315 As previously reported(37), FUCCI2 vectors mCherry hCdt1(30/120)/pCSII EF MCS
316 (DDBJ/EMBL/GenBank, AB512478) and mVenus hGeminin(1/100)/pCSII EF MCS
317 (DDBJ/EMBL/GenBank, AB512479) were purchased from the Riken Brain Science Institute
318 (Japan) and used to generate lentivirus particles by co-transfecting HEK 293TN cells (System
319 Biosciences) with packaging (psPAX2, Addgene plasmid, #12260) and envelope (pMD2.G
320 (Addgene plasmid, #12259) plasmids. The supernatant was collected by centrifuging (Beckman
321 L7-55 with SW32Ti rotor) at 22,000 rpm for 3h at 4 °C. MDA-MB-231 and MCF-7 breast cancer
322 cell lines were first transfected with mVenus hGeminin (1/110) (multiplicity of infection (MOI) of
323 six and five, respectively) followed by mCherry hCdt1 (30/120) at an MOI of three. Verification of
324 successful transduction and subsequent sorting of stably expressing mVenus and mCherry cell lines
325 were perform using flow cytometry (FACSAriaTM II, Becton Dickinson).

Inhibition, RNA interference and drug response experiments

327 For inhibition experiments, the following small molecule and inhibitors were used:
328 MEK/ERK inhibitor PD98059 (10 mM, Focus Biomolecules), JNKinhibitor SP600125 (10 mM,
329 Focus Biomolecules) and PI3K/Akt inhibitor LY294002 (10 mM, Focus Biomolecules). The
330 inhibitors were mixed with culture medium and refreshed every 2-3 days. To knock down FHL2,
331 MDA-MB-231 cells were transfected with two different FHL2-targeting small interfering RNAs
332 (Silencer siRNA, Invitrogen) or non-targeting siRNA (Stealth RNAi negative control, Invitrogen)
333 using Lipofectamine RNAiMAX Reagent (Invitrogen), diluted in Opti-MEM reduced serum

medium (Gibco) for a final concentration of 10-20 nM. Cells were transfected 2-3 days before encapsulation following manufacturer's instructions. To assess MDA-MB-231 response to chemotherapy, Paclitaxel (Tokyo Chemical Industry) was diluted at 0.01, 0.1 and 0.5 mM and added to the culture medium after 3-5 days post-encapsulation for a drug treatment of 2 days. The highest concentration tested contained around 1% (v/v) of DMSO, which was used as vehicle medium and didn't show any negative effect on cell viability.

Immunofluorescence staining

Gels with encapsulated cells were washed (3x) with PBS and fixed with 4% paraformaldehyde (PFA, Boster, #AR1068) for 30 min at room temperature, (3x) washed with 3% w/v bovine serum albumin (BSA, Sigma Aldrich), permeabilized with 0.1 % w/v Triton X 100 (Sigma-Aldrich, #T8787) for 15 min with a final washing (3x) step with 3% BSA. Whole-mount primary antibody staining was performed at 4 °C overnight, diluted in a 3% BSA+0.1% Triton X 100 buffer solution under mild shaking. The gels were then washed (3x) with 3% BSA and incubated with secondary antibody at 4 °C overnight with the same dilution buffer under mild shaking. The samples were finally imaged after a last washing step with PBS (3x). The primary antibodies and respective concentrations used in this study are the following: anti-Ki67 (2 µg/mL, ab15580, abcam), anti-p21$^{Cip1/Waf1}$ (0.48 µg/mL, 2947S, Cell Signaling), anti-FHL2 (0.5 µg/mL, HPA006028, Sigma/Prestige Antibodies). The secondary antibodies are: Alexa Fluor 405 (10 µg/mL, ab175651, abcam) and Alexa Fluor 647 (4 µg/mL, A21244, Invitrogen). To stain for nucleus and cytoskeleton, DAPI (1:1000, Roche) and Alexa Fluor 488 Phalloidin (1:50, Invitrogen) were used.

Immunoblot

Cells were first lysed with RIPA buffer (Abcam) for 5 min on ice and then collected in Eppendorf tubes. Protein concentration was calculated following Bradford assay (Bradford reagent, Sigma-Aldrich). A 1:50 mixture of β-mercaptoethanol (Acros Organics) and 2x Tricine sample buffer (Bio-Rad) was added at a 1:1 volume to the cell lysates. The mixture was then heated to 95 °C for 5 min and loaded into pre-cast polyacrylamide gels (Mini-PROTEAN TGX, Bio-Rad) for electrophoresis in TGS buffer (Bio-Rad) at 100 V for 30 min, then 200 V for 30 min (Mini-PROTEAN Tetra System, Bio-Rad). Proteins in the gels were then blotted onto to a PVDF membrane (BioTrace, PALL) at 150 V for 90 min in ice-cold transfer buffer (1:5 volume of 100% Methanol in TGS buffer). Next, the membrane was transferred to TBST buffer (150 mM NacL, 20 mM Tris-base, 0.1% Tween20), blocked in 5% BSA in TBST buffer for 1 h under gentle shaking, washed in TBST (3x) and incubated with primary antibodies diluted in 1% BSA in TBST overnight at 4 °C. After washing with TBST (3x), the membrane was incubated with an HRP-linked secondary antibody for 1 h at room temperature, after which the chemoluminescence substrate (SuperSignal West Pico PLUS, Thermo Scientific) was added before visualizing it with a blot imager (G:BOX Chemi XX6/XX9, Syngene). GAPDH (1:1000, 2118, Cell Signaling) was used as housekeeping gene and HRP-linked (1:1000, 7074, Cell Signaling) as secondary antibody.

Cell retrieval from 3D gels

For RNA sequencing, MDA-MB-231 cells were retrieved from 3D alginate stiff, soft and 3D Matrigel. Briefly, alginate hydrogels were incubated with alginate lyase (2mg/mL, Sigma Aldrich, A1603) in HBSS (ThermoFisher, 14185045) for 30 min at 37 °C with three mixture steps every 10 min. For Matrigel, pre-cooled (4°C) HBSS was added and mixed for 5-10 min at room temperature, followed by incubation with Trypsin/EDTA (0.05%/0.02%, PAN Biotech, P10-023100) for 5 min at 37 °C. Cells were then washed twice with HBSS for 5 min. Next, retrieved cells were stained using a LIVE/DEAD fixable cell staining method (ThermoFisher, L34969) following manufacturer's instructions, and viable cells were sorted via FACSAria II flow cytometer (Becton Dickinson). Approximately 1500 sorted cells per sample were then lysed using pre-cooled

382 (4 °C) RLN buffer (0.05 M Tri-HCl pH 8.0, 0.14 M NaCl, 0.0015 M MgCl$_2$, 0.5 % v/v Nonidet P-
383 40/IGEPAL (Sigma Aldrich, 56741) and 1000 U/mL RNase inhibitor (Promega, N2615), 0.001 M
384 DTT) on ice for 5 min. The lysates were then centrifuged with a pre-cooled centrifuge for 2 min at
385 300 x g, the supernatants transferred to -80 °C and stored until further processing.

RNA sequencing and analysis

387 Samples were resuspended in 5 µl 1X NEBNext Cell Lysis Buffer of the NEBNext Single
388 Cell/Low Input RNA Library Prep Kit (NEB, E6420). After 5 min incubation at RT, 2.5X RNA XP
389 Clean Up Beads (Beckman Coulter, A63987) were added to the sample by pipetting up and down.
390 Then, samples were incubated for 5 min at RT, the beads were pelleted on a magnet, the supernatant
391 was removed, the samples were washed twice with 80% ethanol while remaining on the magnet,
392 and finally the beads were resuspended in 8 µl nuclease-free water. The reverse transcription was
393 conducted according to the manual of the NEBNext Single Cell/Low Input RNA Library Prep Kit
394 in the presence of the beads. Next, the beads were pelleted on the magnet and the supernatant was
395 used for the following PCR amplification as described in the manual. Twenty-one PCR cycles were
396 applied, because the RNA concentration was below the detection limit of the Qubit RNA HS Assay
397 Kit (Thermo Fisher, Q23852). The cleanup, quality control, fragmentation, and adapter ligation
398 steps were performed as described in the kit manual. NEBNext Multiplex Oligos for Illumina
399 (Index Primer Set 1) (NEB, 7335S) were used for the final PCR amplification. The fragment length
400 distribution of the final libraries was determined using a 2100 Bioanalyzer Instrument (Agilent)
401 with a High Sensitivity DNA kit (Agilent, 5067-4626). The libraries were quantified by qPCR with
402 the KAPA Library Quantification Kit (Roche, KK4854). The nine samples were divided into two
403 pools (one pool of four samples, the other of five samples) with equimolar amount. The pools were
404 sequenced on an Illumina MiSeq with 2 x 150 bp.

405 After demultiplexing, raw FASTQ data were given to an in-house mRNA analysis pipeline
406 0.9.5.5. BBDuk 38.76(*38*) was used to trim the raw sequence data from soft, 3D matrigel and 3D
407 alginate stiff, deleting any residual adapter sequences and low-quality bases at the ends of each
408 read. BioBloom Tools 2.0.13(*39*) was used to decontaminate reads from the genomes Mus
409 musculus (mm38), Escherichia coli (BL21), Mycoplasma pneumoniae (M129), Sphingobium sp.
410 (SYK-6), Bradyrhizobium japonicum (USDA 110), Pichia pastoris (GS115), Malessia globosa
411 (CBS 7966), Aspergillus fumigatus (Af293), and a set of viral genomes (RefSeq, 5k+ genomes).
412 All reads that did not map exclusively to the transcriptome of hg38 (GENCODE version 27,
413 GRCh38.p10) were labeled as potentially contaminated and were removed from further processing.
414 FastQC 0.11.9(*40*) was used to evaluate sequence quality per sample before as well as after
415 trimming and decontamination. In addition, all samples were examined as a collective with
416 MultiQC 1.8(*41*). Following that, the cleaned sample reads were aligned to the hg38 reference
417 genome using STAR 2.5.1b(*42*). Using featureCounts from Subread 2.0.0, uniquely mapping reads
418 were counted per gene and sample(*43*). Further quality criteria were evaluated, including library
419 complexity (using Preseq 2.0.3(*44*)) and the genomic origin of the reads and the 5'-3'-bias (both
420 using QualiMap 2.2.2d(*45*)). The final counts table of 9 samples were utilized for differential
421 expression analysis.

422 All the subsequent steps after the count tables were performed in R programming language
423 4.0.2 (2020-06-22)(*46*). Matrix table containing gene counts were visualized using Principle
424 Component Analysis (PCA) and t-distributed stochastic neighbor embedding (t-SNE) clustering
425 techniques. For PCA, raw counts were scaled and prcomp function from stats package was
426 employed. tSNE plots were constructed using Rtsne 0.15(*47*). Subsequent steps including Quality
427 Control (QC) analysis, filtering, normalization, feature selection, scaling, regression of unwanted
428 variables were performed using Seurat package 4.0.2(*48*). Default parameters were taken for all
429 used functions unless otherwise mentioned. Normalization was done using 'log.normalize' method
430 with a scale factor of $1x10^{-6}$ to obtain logCPM count values and 2,000 most variable genes were

used for feature selection. Only mitochondrial genes were regressed out during scaling, cell cycle associated genes did not have an effect on the cell-to-cell clustering. "DESeq2" method was applied to do differential expression analysis between the three groups, soft, stiff and matrigel and in addition testing of genes was limited to a logFoldChange (logFC) cutoff of 1. Further, the differentially expressed genes were manually filtered for an adjusted *p-value* of 0.05. Finally, volcano plots were constructed using EnhancedVolcano 1.8.0(*49*). In addition to applying single cell method, Seurat, we also applied pure bulk RNA seq method, DESeq2(*50*), to perform the data analysis of the single cell pool samples. Results from both methods were highly similar including the list of differentially expressed genes, their respective fold changes and adjusted *p*-value. We chose to report results from Seurat due to the zero-inflated count distribution of our data which is typical of single cells than bulk RNA data (Supp.Fig.4).

Gene Set Enrichment Analysis (GSEA) of significantly Differentially Expressed Genes (DEGs) (adjusted *p*-value < 0.05 and |logFC|> 1) into functional categories were performed using Bioconductor packages 1.30.15. GOseq 1.42.0(*51*) and clusterProfiler 3.18.1(*52*) were used, respectively, to conduct Gene Ontology (GO)(*53*) and Kyoto Encyclopedia of Genes and Genomes (KEGG)(*54*) enrichment analyses. All the enrichment plots including GSEA, dot plot and heatmap were made using built-in functions in Seurat package or ggplot2 3.3.3(*55*). Network maps were processed based on the selected enriched GO categories using Cytoscape 3.8.2 and enrichment Map plugin(*56*).

Animal experiment

12-week-old female BALB/c nude mice (CAnN.Cg-Foxn1nu/Crl, Charles River, Sulzfeld, Germany) were acclimatized in the animal facility of the Charité-Universitätsmedizin Berlin and housed with ad libitum access to food and water. Mice injected into the left ventricle of the heart with MDA-MB-231-1833 BoM cells ($5x10^5$ cells in 100 µL ice cold PBS), using a 27G needle, under ultrasound guidance (Vevo2100, FUJIFILM VisualSonics Inc., Canada). The animals received Carprosol (CP-Pharma Handelsgesellschaft mbH, Burgdorf, Germany) and Bupresol (CP-Pharma Handelsgesellschaft mbH, Burgdorf, Germany) as analgesic drugs during and after the injection. The animals were anesthetized using isoflurane (CP-Pharma Handelsgesellschaft mbH, Burgdorf, Germany) and the eyes were protected from drying with Pan-Ophtal gel (Dr. Winzer Pharma GmbH, Berlin, Germany). The mouse was sacrificed after 2 weeks by cervical dislocation. The hind limbs were harvested and fixed with 4% paraformaldehyde (PFA) in phosphate-buffered saline (PBS) for 12 h at 4 °C and stored in PBS until further processing. All animal experiments were carried out according to the policies and procedures approved by local legal research animal welfare representatives (LAGeSo Berlin, G0224/18).

For each mouse, bones of one limb were cold embedded at 4°C in poly(methyl methacrylate) (PMMA) (Technovit 9100, Kulzer, Germany), following the manufacturer's instructions. Briefly, samples were dehydrated in an ascending ethanol series, followed by a xylene washing step, infiltration and embedding in PMMA. The staining was performed on 6 µm thick longitudinal sections using a standard protocol of Haematoxylin and Eosin staining (H & E Rapid kit, Clin-Tech, Surrey, UK). Samples were washed in tap water, followed by staining in Carazzi's double-strength Haematoxylin. After another wash in tap water, the slides were stained in Eosin, rinsed in tap water, dehydrated and mounted. The stained sections were imaged with a Keyence Digital Microscope (VKX-5550E, Keyence, Germany). For immunostaining of the slides, after deplastification and rehydration, antigen retrieval was performed (sodium citrate pH 6.0/ 0.05% Tween20) at 105°C for 15 min, followed by 10 min quenching of endogenous peroxidase activity with 3% hydrogen peroxide (Sigma-Aldrich), and a final blocking was performed with Background Sniper (Biocare Medical, Concord, CA, USA) for 10 min. Primary (FHL2 2 µg/mL and Ki67 2 µg/mL) and secondary antibodies (same as for in vitro immunofluorescence staining) were diluted in Dako antibody diluent (Dako, Germany). Washing steps were done in Dako washing buffer.

480 Slides were then mounted with Vectashield antifade mounting medium (Biozol, Germany)
481 following manufacturer's instructions.

482 Bones of the other limb of the mouse were freeze embedded following the method of the
483 SECTION-LAB Co. Ltd. (Hiroshima, Japan). The samples were dehydrated in an ascending
484 sucrose solution (10%, 20% and 30% in distilled water) for 24 h each at 4°C. Following this, a
485 metal mold was placed in cooled isopropanol and filled with embedding medium (SCEM;
486 SECTION-LAB Co. Ltd.), placing the bone in the middle. Cryosections with a thickness of 20 µm
487 were cut following the Kawamoto method(57) using a cryostat (Leica CM3060S). The section was
488 collected using a Kawamoto film (cryofilm type II C(9)) and later attached to a microscopic slide
489 and stored at -20°C until further use. For immunostaining the slides were blocked with blocking
490 buffer (1%BSA/ 0.1%Tween20 in PBS). Primary and secondary antibodies were diluted in blocking
491 buffer and incubated for at least 4 and 1h at room temperature, respectively. Washing steps (2x for
492 15min) were conducted in washing buffer (0.1%Tween20 in PBS) and distilled water. Slides were
493 then mounted with Dako fluorescence mounting media (S302380-2, Agilent Technologies).

Immunofluorescence staining of human early DCCs in lymph node samples of an M0 breast cancer patient

496 After informed consent (ethics vote number 18-948-101), the sentinel lymph node of an
497 M0-stage breast cancer patient (i.e. with no evidence of distant metastasis) was first divided into
498 two halves and one half examined by histopathology. The other half was disaggregated
499 mechanically (DAKO Medimachine, DAKO) to generate a single-cell suspension. Then,
500 mononuclear cells were isolated using a density gradient centrifugation (60% Percoll solution,
501 Amersham) and plated onto adhesive slides. After sedimentation of the cells, the supernatant was
502 discarded and slides were air-dried and stored at -20°C. For immunofluorescence staining of FHL2
503 and Cytokeratin 8/18/19, the slides were first thawed at RT and moistened with PBS. Cells were
504 fixed with 2% PFA (Sigma, P6148) for 10 min, washed twice with PBS and permeablized with
505 0.05% TritonX100 for 5 min. After two additional washing steps with PBS, cells were blocked with
506 PBS/10% AB serum (#805135, Bio-Rad) for 1.5 hours at RT. Primary antibody incubation with
507 monoclonal mouse anti-human Cytokeratin 8/18/19 (2 µg/mL, clone A45-B/B3, AS Diagnostik)
508 and polyclonal rabbit anti-human FHL2 (2 µg/mL, HPA006028, Sigma/Prestige Antibodies) was
509 performed at 4 °C overnight in PBS/10% AB serum. Following washing with PBS (4x 20 min), the
510 slides were incubated with secondary antibodies, anti-mouse AlexaFluor 488 (5 µg/mL, A11029,
511 Invitrogen) and anti-rabbit AlexaFluor Plus 647 (5 µg/mL, A32733, Invitrogen) and DAPI
512 (1µg/mL, MBD0015, Sigma) in PBS/5% AB serum/2.5% goat serum for 1.5 hours. After washing
513 off the secondary antibodies (PBS 3x 10 min) the slides were mounted with SlowFade™ Glass
514 Soft-set Antifade Mountant (S36917, Invitrogen) and imaged on Zeiss LSM980. Images were
515 processed with ImageJ (v.1.53q) to show the max-z-projections.

Image acquisition and analysis

517 Live-cell imaging was conducted in a stage top incubator (Okolab, UNO-T-H-CO_2)
518 mounted on an inverted epifluorescence microscope (Zeiss, AxioObserver 7) and a 10x, 0.3 NA
519 objective at 37 °C and 5% CO_2. Images were recorded every 6 h for 4-5 days. For FUCCI2 image
520 analysis, live-cell imaging of cells on 2D TCP or 3D hydrogels was performed and mCherry and
521 mVenus fluorescence signals were recorded every 6 h. Briefly, after choosing a focus plane at the
522 beginning of the experiment for each field of view, a z-stack of this region/20 µm was acquired
523 around this position, and phase contrast as well as fluorescence images were recorded.

524 At the end of the experiment, *in situ* viability staining with calcein was performed and the
525 same z-stack/middle-focus plain as the final timelapse acquisition step was acquired. This allowed
526 longitudinal correlation of viability at the end of the experiment with cell cycle progression over
527 the course of the experiment. The number of cdt1- cells at the final timepoint was counted as the

528 difference between FUCCI2+ cells (cells that either express mCherry or mVenus) at the initial and
529 the last timepoint, with additional reference to phase contrast images. Next, viable (calcein+) single
530 cells were counted and the dynamics of their FUCCI2 fluorescence signal extracted using a semi-
531 automated custom-made MATLAB script. To do this, viable cells were picked and tracked over
532 and mean nuclear FUCCI2 intensity was extracted.

533 To quantify viability, projected images were thresholded for each channel corresponding to
534 viable (calcein +) or dead (EthD-1) cells using a counting custom-made MATLAB script. To
535 quantify immunofluorescence, images were first thresholded for nucleus (DAPI) and cytoskeleton
536 (F-Actin) to localize single cells, after which the immunofluorescence signal intensity within the
537 defined boundaries was extracted for each cell. The background signal of negatively-stained
538 samples was used to define the threshold for positive cells. The described process was performed
539 using an automated custom-made MATLAB script.

540 To quantify p21 and FHL2 localization, a Leica SP8 confocal microscope with 63x, 1.4 NA
541 oil-immersion objective was used. Briefly, images were thresholded for nucleus (DAPI) and
542 cytoskeleton (F-Actin) to define the respective intracellular regions, after which p21 or FHL2
543 average intensity within each region was recorded. The described process was performed using an
544 automated custom-made MATLAB script.

545 Images of human tissue samples from patients with primary breast cancer were obtained
546 from the Human Protein Atlas (www.proteinatlas.org)(*58*). Samples with strong FHL2 intensity
547 were selected, of which the localization was already designated as being either nuclear or
548 cytoplasmic.

Statistical analysis

550 For statistical comparison between two groups, two-tailed student's t-test or Mann-Whitney
551 U-test were performed for normally-distributed or non-parametric groups, respectively (*: $p \leq 0.05$,
552 **: $p \leq 0.01$, ***: $p \leq 0.001$, ****: $p \leq 0.0001$). One-way Anova with Tukey's correction or Kruskal-
553 Wallis test with Dunn's correction were conducted for multiple-group comparison. Error bars
554 indicate mean and standard deviation used for fraction graphs. Datasets shown as box plots with
555 median, for 25th to 75th percentiles and whiskers for minimum and maximum used for ratio graphs.
556 Violin plots show dashed lines for median and dotted lines for the two quartile lines, used for
557 fluorescence intensity graphs. GraphPad Prism 8 software was used to plot the data and for
558 statistical analysis.

References

1. C. A. Klein, Cancer progression and the invisible phase of metastatic colonization. *Nat. Rev. Cancer*. **20**, 681–694 (2020).
2. C. M. Ghajar, Metastasis prevention by targeting the dormant niche. *Nat. Rev. Cancer*. **15**, 238–247 (2015).
3. M. Montagner, E. Sahai, In vitro Models of Breast Cancer Metastatic Dormancy. *Front. Cell Dev. Biol.* **8**, 1–10 (2020).
4. S. Galarza, A. J. Crosby, C. Pak, S. R. Peyton, Control of Astrocyte Quiescence and Activation in a Synthetic Brain Hydrogel. *Adv. Healthc. Mater.* **9**, 1901419 (2020).
5. M. Quarta, J. O. Brett, R. DiMarco, A. De Morree, S. C. Boutet, R. Chacon, M. C. Gibbons, V. A. Garcia, J. Su, J. B. Shrager, S. Heilshorn, T. A. Rando, An artificial niche preserves the quiescence of muscle stem cells and enhances their therapeutic efficacy. *Nat. Biotechnol.* **34**, 752–759 (2016).

6. C. M. Madl, B. L. LeSavage, R. E. Dewi, C. B. Dinh, R. S. Stowers, M. Khariton, K. J. Lampe, D. Nguyen, O. Chaudhuri, A. Enejder, S. C. Heilshorn, Maintenance of neural progenitor cell stemness in 3D hydrogels requires matrix remodelling. *Nat. Mater.* **16**, 1233–1242 (2017).

7. A. Roch, S. Giger, M. Girotra, V. Campos, N. Vannini, O. Naveiras, S. Gobaa, M. P. Lutolf, Single-cell analyses identify bioengineered niches for enhanced maintenance of hematopoietic stem cells. *Nat. Commun.* **8**, 221 (2017).

8. C. Yang, M. W. Tibbitt, L. Basta, K. S. Anseth, Mechanical memory and dosing influence stem cell fate. *Nat. Mater.* **13**, 645–652 (2014).

9. S. Khetan, M. Guvendiren, W. R. Legant, D. M. Cohen, C. S. Chen, J. A. Burdick, Degradation-mediated cellular traction directs stem cell fate in covalently crosslinked three-dimensional hydrogels. *Nat. Mater.* **12**, 458–465 (2013).

10. S. Pradhan, J. H. Slater, Tunable hydrogels for controlling phenotypic cancer cell states to model breast cancer dormancy and reactivation. *Biomaterials*. **215**, 119177 (2019).

11. S. Nam, V. K. Gupta, H. Lee, J. Y. Lee, K. M. Wisdom, S. Varma, E. M. Flaum, C. Davis, R. B. West, O. Chaudhuri, Cell cycle progression in confining microenvironments is regulated by a growth-responsive TRPV4-PI3K/Akt-p27 Kip1 signaling axis. *Sci. Adv.* **5**, eaaw6171 (2019).

12. O. Chaudhuri, S. T. Koshy, C. Branco da Cunha, J.-W. Shin, C. S. Verbeke, K. H. Allison, D. J. Mooney, Extracellular matrix stiffness and composition jointly regulate the induction of malignant phenotypes in mammary epithelium. *Nat. Mater.* **13**, 970–978 (2014).

13. B. R. Seo, P. Bhardwaj, S. Choi, J. Gonzalez, R. C. Andresen Eguiluz, K. Wang, S. Mohanan, P. G. Morris, B. Du, X. K. Zhou, L. T. Vahdat, A. Verma, O. Elemento, C. A. Hudis, R. M. Williams, D. Gourdon, A. J. Dannenberg, C. Fischbach, Obesity-dependent changes in interstitial ECM mechanics promote breast tumorigenesis. *Sci. Transl. Med.* **7**, 301ra130-301ra130 (2015).

14. A. Lueckgen, D. S. Garske, A. Ellinghaus, D. J. Mooney, G. N. Duda, A. Cipitria, Enzymatically-degradable alginate hydrogels promote cell spreading and in vivo tissue infiltration. *Biomaterials*. **217**, 119294 (2019).

15. A. Sakaue-Sawano, H. Kurokawa, T. Morimura, A. Hanyu, H. Hama, H. Osawa, S. Kashiwagi, K. Fukami, T. Miyata, H. Miyoshi, T. Imamura, M. Ogawa, H. Masai, A. Miyawaki, Visualizing Spatiotemporal Dynamics of Multicellular Cell-Cycle Progression. *Cell*. **132**, 487–498 (2008).

16. A. Sakaue-Sawano, T. Kobayashi, K. Ohtawa, A. Miyawaki, Drug-induced cell cycle modulation leading to cell-cycle arrest, nuclear mis-segregation, or endoreplication. *BMC Cell Biol.* **12**, 2 (2011).

17. S. Gookin, M. Min, H. Phadke, M. Chung, J. Moser, I. Miller, D. Carter, S. L. Spencer, A map of protein dynamics during cell-cycle progression and cell-cycle exit. *PLOS Biol.* **15**, e2003268 (2017).

18. A. Karimian, Y. Ahmadi, B. Yousefi, Multiple functions of p21 in cell cycle, apoptosis and transcriptional regulation after DNA damage. *DNA Repair (Amst).* **42**, 63–71 (2016).

19. B. M. Baker, C. S. Chen, Deconstructing the third dimension – how 3D culture microenvironments alter cellular cues. *J. Cell Sci.* **125**, 3015–3024 (2012).

20. B. T. Martin, K. Kleiber, V. Wixler, M. Raab, B. Zimmer, M. Kaufmann, K. Strebhardt, FHL2 Regulates Cell Cycle-Dependent and Doxorubicin-Induced p21Cip1/Waf1 Expression in Breast Cancer Cells. *Cell Cycle*. **6**, 1779–1788 (2007).

21. N. Nakazawa, A. R. Sathe, G. V. Shivashankar, M. P. Sheetz, Matrix mechanics controls FHL2 movement to the nucleus to activate p21 expression. *Proc. Natl. Acad. Sci.* **113**, E6813–E6822 (2016).

22. J. Y. Lee, J. K. Chang, A. A. Dominguez, H. Lee, S. Nam, J. Chang, S. Varma, L. S. Qi, R.

B. West, O. Chaudhuri, YAP-independent mechanotransduction drives breast cancer progression. *Nat. Commun.* **10**, 1848 (2019).

23. O. Y. Dudaryeva, A. Bucciarelli, G. Bovone, F. Huwyler, S. Jaydev, N. Broguiere, M. Al-Bayati, M. Lütolf, M. W. Tibbitt, 3D Confinement Regulates Cell Life and Death. *Adv. Funct. Mater.* **i**, 2104098 (2021).

24. K. Kleiber, K. Strebhardt, B. T. Martin, The biological relevance of FHL2 in tumour cells and its role as a putative cancer target. *Anticancer Res.* **27**, 55–62 (2007).

25. J. Albrengues, M. A. Shields, D. Ng, C. G. Park, A. Ambrico, M. E. Poindexter, P. Upadhyay, D. L. Uyeminami, A. Pommier, V. Küttner, E. Bružas, L. Maiorino, C. Bautista, E. M. Carmona, P. A. Gimotty, D. T. Fearon, K. Chang, S. K. Lyons, K. E. Pinkerton, L. C. Trotman, M. S. Goldberg, J. T. H. Yeh, M. Egeblad, Neutrophil extracellular traps produced during inflammation awaken dormant cancer cells in mice. *Science (80-.).* **361**, eaao4227 (2018).

26. D. Barkan, H. Kleinman, J. L. Simmons, H. Asmussen, A. K. Kamaraju, M. J. Hoenorhoff, Z. -y. Liu, S. V. Costes, E. H. Cho, S. Lockett, C. Khanna, A. F. Chambers, J. E. Green, Inhibition of Metastatic Outgrowth from Single Dormant Tumor Cells by Targeting the Cytoskeleton. *Cancer Res.* **68**, 6241–6250 (2008).

27. J. A. Aguirre Ghiso, Inhibition of FAK signaling activated by urokinase receptor induces dormancy in human carcinoma cells in vivo. *Oncogene.* **21**, 2513–2524 (2002).

28. T. Shibue, R. A. Weinberg, Integrin 1-focal adhesion kinase signaling directs the proliferation of metastatic cancer cells disseminated in the lungs. *Proc. Natl. Acad. Sci.* **106**, 10290–10295 (2009).

29. E. E. Er, M. Valiente, K. Ganesh, Y. Zou, S. Agrawal, J. Hu, B. Griscom, M. Rosenblum, A. Boire, E. Brogi, F. G. Giancotti, M. Schachner, S. Malladi, J. Massagué, Pericyte-like spreading by disseminated cancer cells activates YAP and MRTF for metastatic colonization. *Nat. Cell Biol.* **20**, 966–978 (2018).

30. M. Werner-Klein, A. Grujovic, C. Irlbeck, M. Obradović, M. Hoffmann, H. Koerkel-Qu, X. Lu, S. Treitschke, C. Köstler, C. Botteron, K. Weidele, C. Werno, B. Polzer, S. Kirsch, M. Gužvić, J. Warfsmann, K. Honarnejad, Z. Czyz, G. Feliciello, I. Blochberger, S. Grunewald, E. Schneider, G. Haunschild, N. Patwary, S. Guetter, S. Huber, B. Rack, N. Harbeck, S. Buchholz, P. Rümmele, N. Heine, S. Rose-John, C. A. Klein, Interleukin-6 trans-signaling is a candidate mechanism to drive progression of human DCCs during clinical latency. *Nat. Commun.* **11**, 4977 (2020).

31. B. Gabriel, D.-C. Fischer, M. Orlowska-Volk, A. zur Hausen, R. Schüle, J. M. Müller, A. Hasenburg, Expression of the Transcriptional Coregulator FHL2 in Human Breast Cancer: A Clinicopathologic Study. *J. Soc. Gynecol. Investig.* **13**, 69–75 (2006).

32. A. Lueckgen, D. S. Garske, A. Ellinghaus, D. J. Mooney, G. N. Duda, A. Cipitria, Enzymatically-degradable alginate hydrogels promote cell spreading and in vivo tissue infiltration. *Biomaterials*. **217**, 119294 (2019).

33. S. T. Gould, N. J. Darling, K. S. Anseth, Small peptide functionalized thiol–ene hydrogels as culture substrates for understanding valvular interstitial cell activation and de novo tissue deposition. *Acta Biomater.* **8**, 3201–3209 (2012).

34. A. J. Minn, G. P. Gupta, P. M. Siegel, P. D. Bos, W. Shu, D. D. Giri, A. Viale, A. B. Olshen, W. L. Gerald, J. Massagué, Genes that mediate breast cancer metastasis to lung. *Nature*. **436**, 518–524 (2005).

35. Y. Kang, P. M. Siegel, W. Shu, M. Drobnjak, S. M. Kakonen, C. Cordón-Cardo, T. A. Guise, J. Massagué, A multigenic program mediating breast cancer metastasis to bone. *Cancer Cell*. **3**, 537–549 (2003).

36. V. Ponomarev, M. Doubrovin, I. Serganova, J. Vider, A. Shavrin, T. Beresten, A. Ivanova, L. Ageyeva, V. Tourkova, J. Balatoni, W. Bornmann, R. Blasberg, J. Gelovani Tjuvajev, A

novel triple-modality reporter gene for whole-body fluorescent, bioluminescent, and nuclear noninvasive imaging. *Eur. J. Nucl. Med. Mol. Imaging*. **31**, 740–751 (2004).

37. H. M. Taïeb, D. S. Garske, J. Contzen, M. Gossen, L. Bertinetti, T. Robinson, A. Cipitria, Osmotic pressure modulates single cell cycle dynamics inducing reversible growth arrest and reactivation of human metastatic cells. *Sci. Rep.* **11**, 13455 (2021).

38. BBtools software suite. *JGI DataScience* (2019).

39. J. Chu, S. Sadeghi, A. Raymond, S. D. Jackman, K. M. Nip, R. Mar, H. Mohamadi, Y. S. Butterfield, A. G. Robertson, I. Birol, BioBloom tools: fast, accurate and memory-efficient host species sequence screening using bloom filters. *Bioinformatics*. **30**, 3402–3404 (2014).

40. S. Andrews, FastQC: A Quality Control Tool for High Throughput Sequence Data. (2010).

41. P. Ewels, M. Magnusson, S. Lundin, M. Käller, MultiQC: summarize analysis results for multiple tools and samples in a single report. *Bioinformatics*. **32**, 3047–3048 (2016).

42. A. Dobin, C. A. Davis, F. Schlesinger, J. Drenkow, C. Zaleski, S. Jha, P. Batut, M. Chaisson, T. R. Gingeras, STAR: ultrafast universal RNA-seq aligner. *Bioinformatics*. **29**, 15–21 (2013).

43. Y. Liao, G. K. Smyth, W. Shi, The Subread aligner: fast, accurate and scalable read mapping by seed-and-vote. *Nucleic Acids Res.* **41**, e108–e108 (2013).

44. C. Deng, T. Daley, A. Smith, Applications of species accumulation curves in large-scale biological data analysis. *Quant. Biol.* **3**, 135–144 (2015).

45. K. Okonechnikov, A. Conesa, F. García-Alcalde, Qualimap 2: advanced multi-sample quality control for high-throughput sequencing data. *Bioinformatics*. **32**, btv566 (2015).

46. R. C. Team, R: A Language and Environment for Statistical Computing. (2020).

47. L. van der Maaten, Accelerating t-SNE using Tree-Based Algorithms. *J. Mach. Learn. Res.* **15**, 3221–3245 (2014).

48. Y. Hao, S. Hao, E. Andersen-Nissen, W. M. Mauck, S. Zheng, A. Butler, M. J. Lee, A. J. Wilk, C. Darby, M. Zager, P. Hoffman, M. Stoeckius, E. Papalexi, E. P. Mimitou, J. Jain, A. Srivastava, T. Stuart, L. M. Fleming, B. Yeung, A. J. Rogers, J. M. McElrath, C. A. Blish, R. Gottardo, P. Smibert, R. Satija, Integrated analysis of multimodal single-cell data. *Cell*. **184**, 3573-3587.e29 (2021).

49. K. Blighe, S. Rana, M. Lewis, EnhancedVolcano: Publication-ready volcano plots with enhanced colouring and labeling. (2018).

50. M. I. Love, W. Huber, S. Anders, Moderated estimation of fold change and dispersion for RNA-seq data with DESeq2. *Genome Biol.* **15**, 550 (2014).

51. M. D. Young, M. J. Wakefield, G. K. Smyth, A. Oshlack, Gene ontology analysis for RNA-seq: accounting for selection bias. *Genome Biol.* **11**, R14 (2010).

52. G. Yu, L.-G. Wang, Y. Han, Q.-Y. He, clusterProfiler: an R Package for Comparing Biological Themes Among Gene Clusters. *Omi. A J. Integr. Biol.* **16**, 284–287 (2012).

53. M. Ashburner, C. A. Ball, J. A. Blake, D. Botstein, H. Butler, J. M. Cherry, A. P. Davis, K. Dolinski, S. S. Dwight, J. T. Eppig, M. A. Harris, D. P. Hill, L. Issel-Tarver, A. Kasarskis, S. Lewis, J. C. Matese, J. E. Richardson, M. Ringwald, G. M. Rubin, G. Sherlock, Gene Ontology: tool for the unification of biology. *Nat. Genet.* **25**, 25–29 (2000).

54. M. Kanehisa, S. Goto, M. Furumichi, M. Tanabe, M. Hirakawa, KEGG for representation and analysis of molecular networks involving diseases and drugs. *Nucleic Acids Res.* **38**, D355–D360 (2010).

55. H. Wickham, *ggplot2: Elegant Graphics for Data Analysis* (Springer-Verlag New York, 2016).

56. D. Merico, R. Isserlin, O. Stueker, A. Emili, G. D. Bader, Enrichment Map: A Network-Based Method for Gene-Set Enrichment Visualization and Interpretation. *PLoS One*. **5**, e13984 (2010).

57. T. Kawamoto, Use of a new adhesive film for the preparation of multi-purpose fresh-frozen

sections from hard tissues, whole-animals, insects and plants. *Arch. Histol. Cytol.* **66**, 123–143 (2003).

58. M. Uhlen, C. Zhang, S. Lee, E. Sjöstedt, L. Fagerberg, G. Bidkhori, R. Benfeitas, M. Arif, Z. Liu, F. Edfors, K. Sanli, K. von Feilitzen, P. Oksvold, E. Lundberg, S. Hober, P. Nilsson, J. Mattsson, J. M. Schwenk, H. Brunnström, B. Glimelius, T. Sjöblom, P.-H. Edqvist, D. Djureinovic, P. Micke, C. Lindskog, A. Mardinoglu, F. Ponten, A pathology atlas of the human cancer transcriptome. *Science (80-.).* **357**, eaan2507 (2017).

59. Cortazar, A. R. *et al.* CANCERTOOL: A Visualization and Representation Interface to Exploit Cancer Datasets. *Cancer Res.* **78**, 6320–6328 (2018).

60. Chen, F., Chandrashekar, D. S., Varambally, S. & Creighton, C. J. Pan-cancer molecular subtypes revealed by mass-spectrometry-based proteomic characterization of more than 500 human cancers. *Nat. Commun.* **10**, 5679 (2019).

61. Chandrashekar, D. S. *et al.* UALCAN: An update to the integrated cancer data analysis platform. *Neoplasia* **25**, 18–27 (2022).

62. Chandrashekar, D. S. *et al.* UALCAN: A Portal for Facilitating Tumor Subgroup Gene Expression and Survival Analyses. *Neoplasia* **19**, 649–658 (2017).

63. Lánczky, A. & Győrffy, B. Web-Based Survival Analysis Tool Tailored for Medical Research (KMplot): Development and Implementation. *J. Med. Internet Res.* **23**, e27633 (2021).

64. Győrffy, B. Survival analysis across the entire transcriptome identifies biomarkers with the highest prognostic power in breast cancer. *Comput. Struct. Biotechnol. J.* **19**, 4101–4109 (2021).

Acknowledgments

Competing interests: CAK is member of the SAB of HiberCell.

772   **Figures**

773
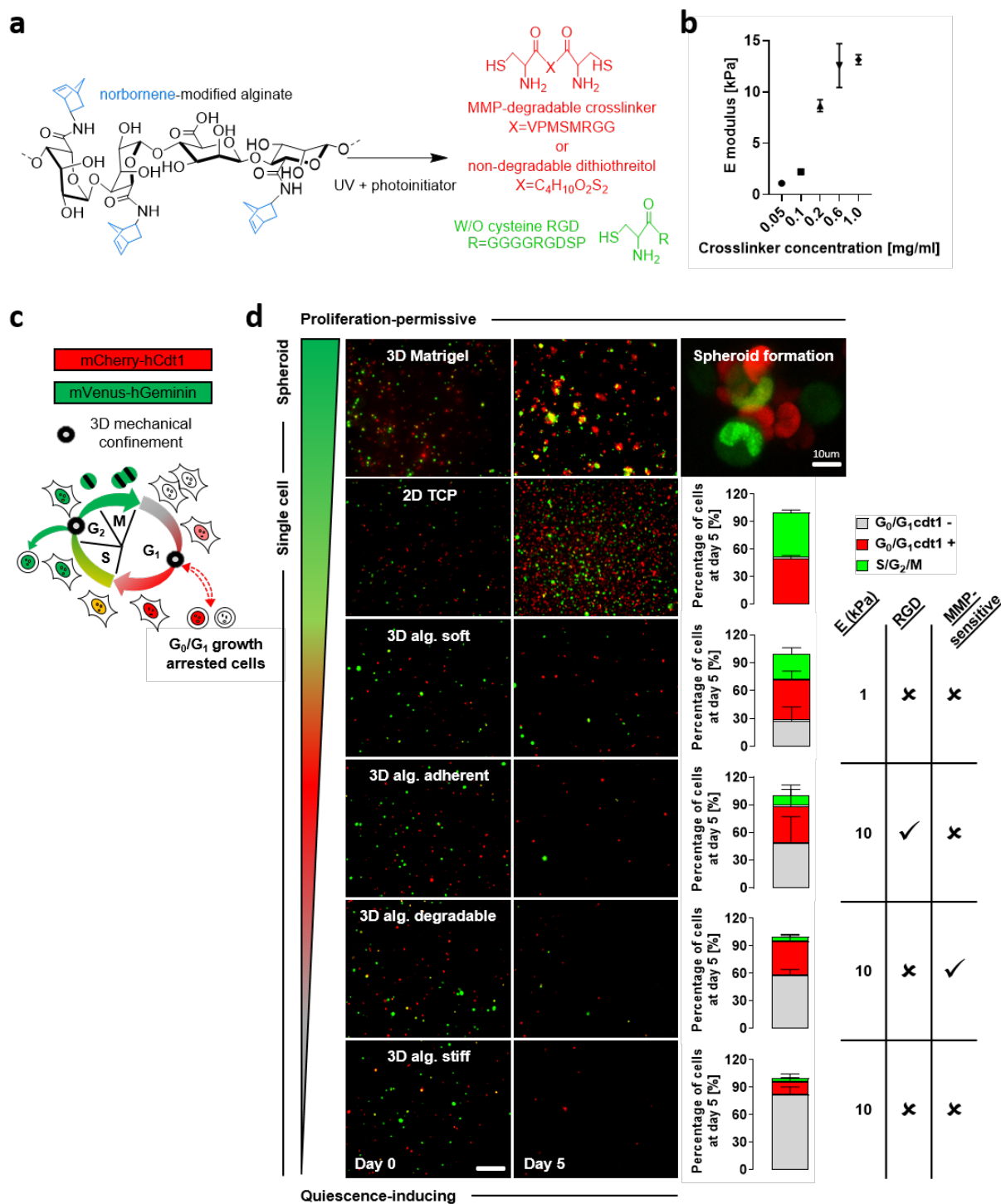
774   **Fig. 1 3D mechanical confinement via covalently-crosslinked alginate yields distinct**
775   **fractions and populations of growth-arrested cells based on hydrogel composition. a)**
776   Bis-cysteine enzymatically (MMP) degradable peptide or non-degradable dithiothreitol
777   (DTT) (red) crosslink with norbornene-modified alginate (blue) in the presence or absence
778   of cysteine-coupled RGD molecules (green). **b)** Frequency sweep of norbornene-modified
779   alginate (no RGD) with different concentrations of DTT crosslinker yields a range of
780   stiffness (Elastic/Young's moduli) (n=3). **c)** Diagram of FUCCI2 cell cycle reporter activity

$(G_0/G_1$=mCherry-hCdt1 and S/G_2/M=mVenus-hGeminin). The cartoon was adapted from Sakaue-Sawano et al.[15], Copyright (2008), with permission from Elsevier. **d)** Time lapse imaging (5 days) of MDA-FUCCI2 cells within a range of proliferation-permissive and quiescence-inducing hydrogels with distinct stiffness, adhesion and degradation properties (right-hand side table). Representative time lapse fluorescence maximum projections at day 0 and day 5, scale bar equals 200 μm. Scale bar equals 10 μm for 3D Matrigel spheroid image. Percentage bar plots show fraction of cell cycle distribution at day 5 for different experimental groups. Error bars indicate mean and standard deviation (n≥3 gels for 82 to 453 cells).

812

Dynamics of 3D mechanical confinement-induced dormancy
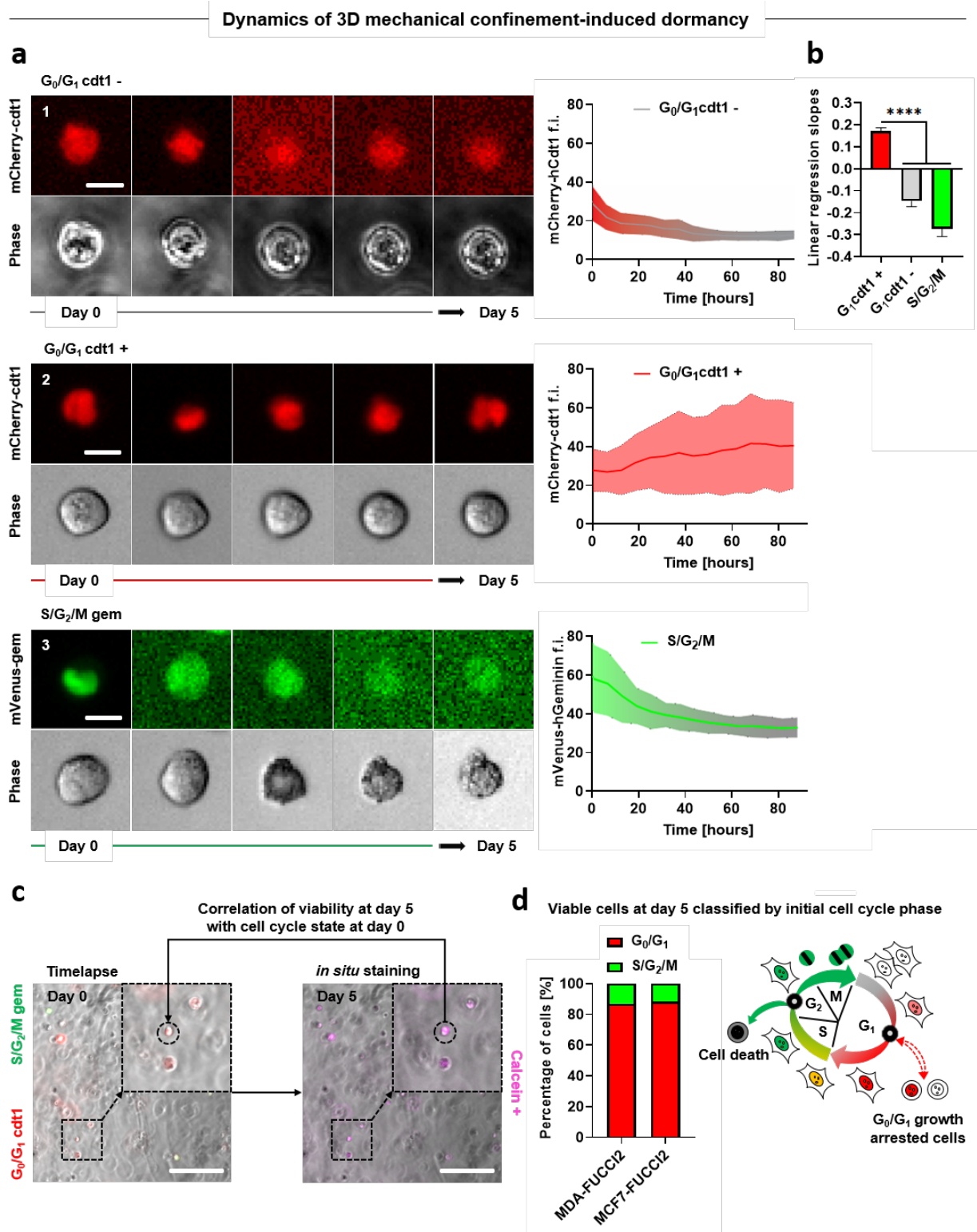
Fig. 2 Dynamics of cell cycle and viability correlation reveal that G_0/G_1 cells are substantially more resistant to 3D mechanical confinement than cells in the $S/G_2/M$ phase. a) Representative time lapse images of single MDA-FUCCI2 cells in 3D alginate stiff hydrogels with respective single cell longitudinal tracking of mCherry-hCdt1 and mVenus-hGeminin fluorescence intensity (f.i.). Center trace and shaded area indicate mean and standard deviation (n≥15 cells). Scale bar equals 10 μm. **b)** Comparison of linear

819 regression slopes from f.i. tracking graph. Kruskal–Wallis test with Dunn's correction
820 ****p<0.0001. **c)** Experimental workflow for longitudinal correlation of FUCCI2 initial
821 cell cycle state within 3D alginate stiff hydrogels and viability after 5 days of encapsulation.
822 Cells were stained *in situ* for viability after 5 days time lapse and the selected cells (calcein+)
823 were tracked back to their initial cell cycle state (time of encapsulation). Scale bar equals
824 200 μm. **d)** Percentage bar plots show fraction of viable cells with respect to their initial cell
825 cycle state for MDA-FUCCI2 and MCF7-FUCCI2 cells (n≥241 cells pooled from 3
826 independent experiments). Diagram of cell cycle progression under 3D mechanical
827 confinement, revealing growth arrest and higher resilience for cells in G_0/G_1 and death for
828 cells in $S/G_2/M$. The cartoon was adapted from Sakaue-Sawano et al.[15], Copyright (2008),
829 with permission from Elsevier.

830

831

832

833

834

835

836

837
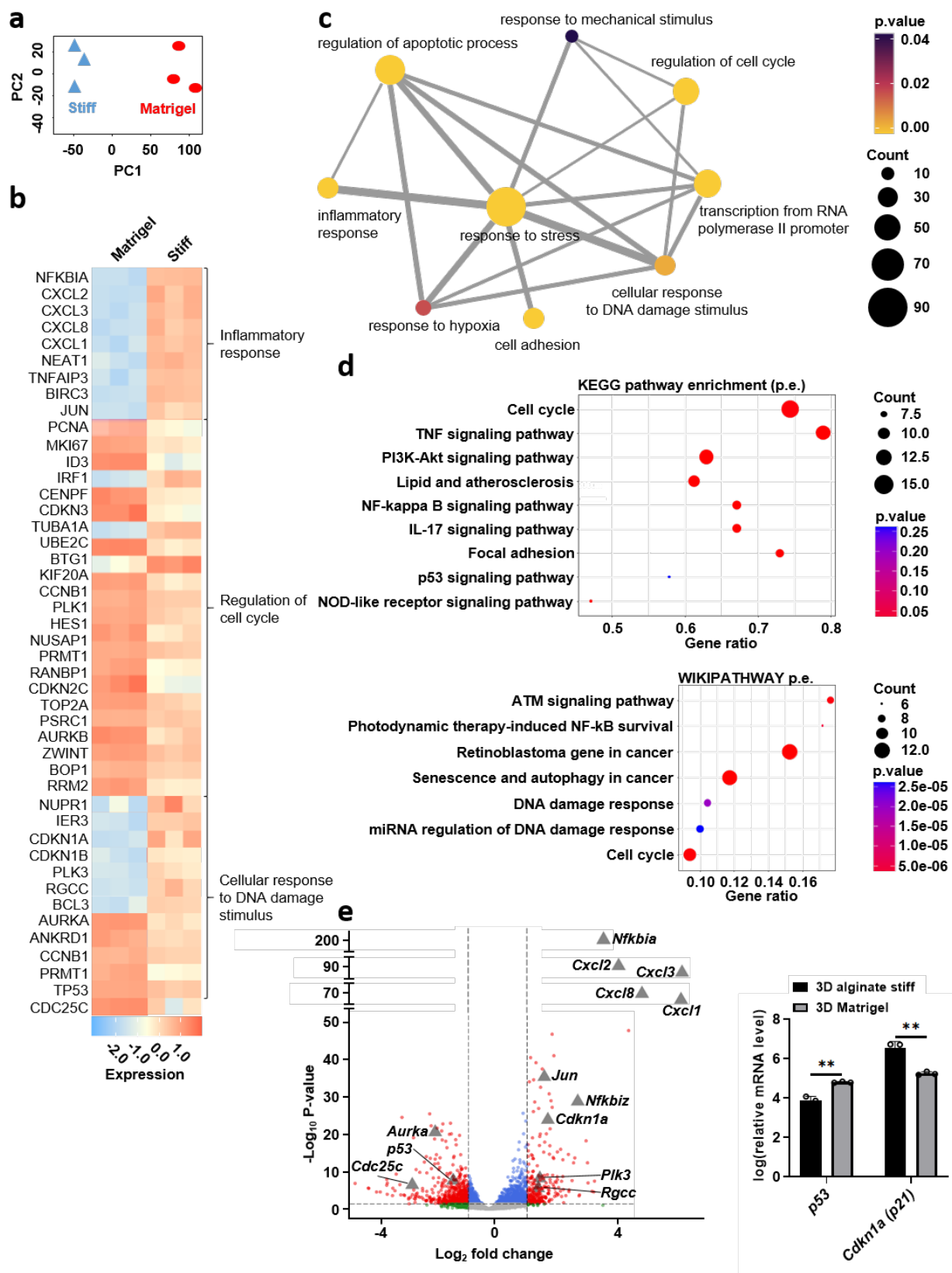
838

839

840

841

842

843

844

845

846

847

848

Fig. 3 Gene expression analysis of cells in 3D alginate stiff compared to 3D Matrigel.
a) Principal-component analysis (PCA) based on all expressed genes between 3D alginate stiff and 3D Matrigel groups acquired from RNA sequencing (n=3 for each condition).

b) Heat map of selected differentially expressed genes involved in inflammatory response, regulation of cell cycle and cellular response to DNA damage stimulus. **c)** Network map of selected biological processes most enriched in 3D alginate compared to 3D Matrigel. Node size, node color and edge width represent number of genes, *p*-value from enrichment analysis and overlap of number of genes between two gene sets, respectively. **d)** Selected top differentially regulated pathways from Gene-set-enrichment analysis (GSEA) on differentially expressed genes between cells grown in 3D alginate stiff and 3D Matrigel according to KEGG and WIKIPATHWAY databases. **e)** Volcano plot of differentially expressed genes between 3D alginate stiff and 3D Matrigel. Grey triangles mark genes of interest associated with inflammation and DNA-damage pathways (grey dots=not significant, green dots= significant absolute log(base2) fold change of > 1, blue dots= significant *p-value* of < 0.05, red=significant absolute log(base2) fold change of > 1 and *p-value* <0.05 from a total of 9426 entries). Relative mRNA levels of p53 and cdkn1a (p21) (n=3 for each condition). Student's *t*-test **p≤0.01. Error bars indicate mean and standard deviation.
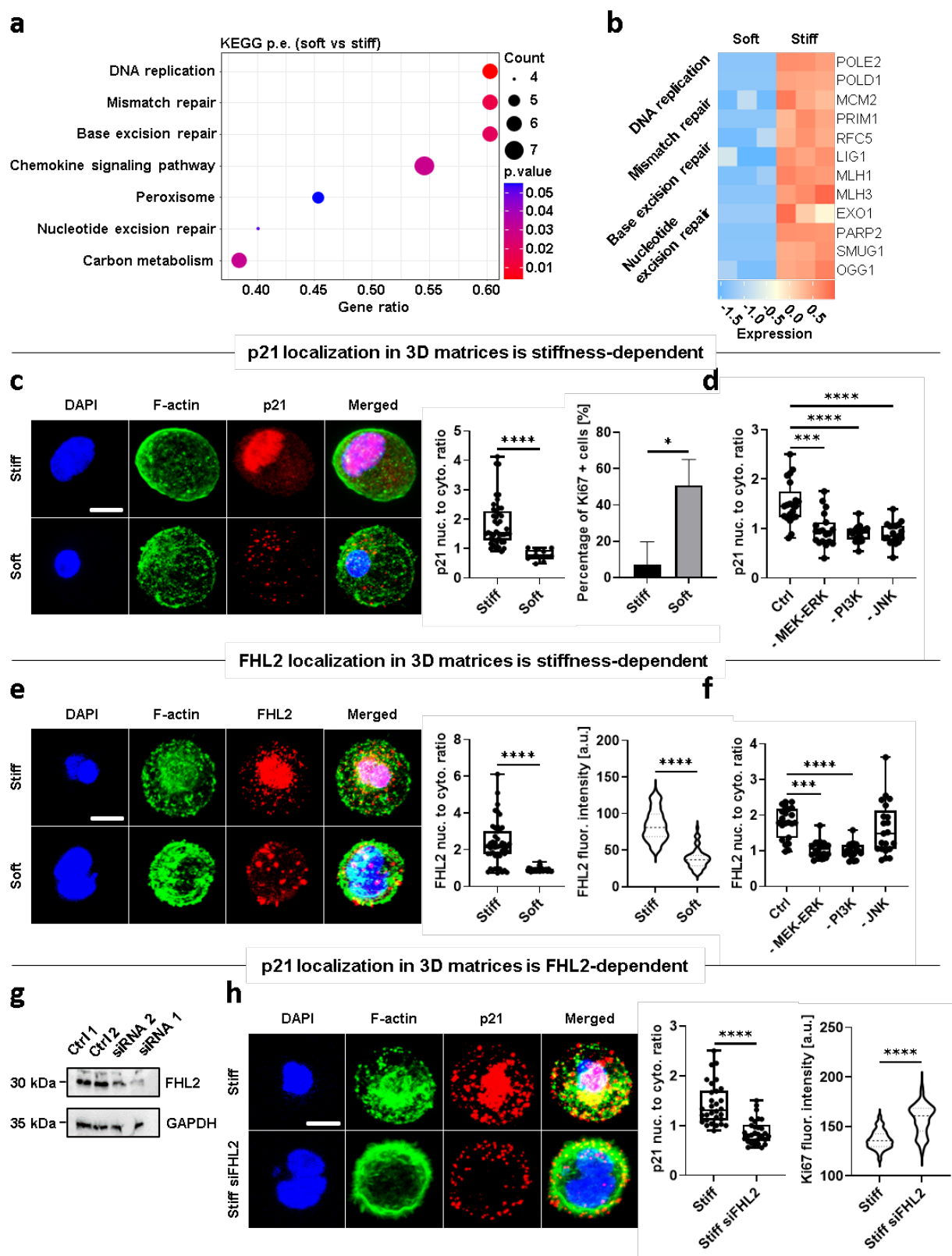
Fig. 4 p21 and FHL2 localization in 3D matrices is stiffness-dependent and FHL2 mediates p21 localization and Ki67 expression. a) Selected top differentially regulated pathways from GSEA based on differentially expressed genes between cells grown in soft vs. stiff alginate hydrogels. **b)** Heat map of differentially expressed genes (soft vs. stiff)

from DNA damage and repair pathways. **c)** Representative confocal images of p21 localization and quantification of its nuclear-to-cytoplasmic ratio (n=3 gels for 10 to 42 cells) for MDA231 cells within 3D stiff and soft alginate hydrogels after 7 days of encapsulation (blue=DAPI, green=F-Actin, red=p21). Scale bar equals 10 μm, Mann-Whitney *U*-test ****p<0.0001. Fraction of Ki67-positive cells (n=3 gels for 28 to 628 cells), student's *t*-test *p<0.05. **d)** Quantification of p21 localization in 3D alginate stiff hydrogels after 7 days in the presence or absence of indicated inhibitors (n≥19 cells). Student's *t*-test with respect to control group (3D alginate stiff) ***p<0.001 and ****p<0.0001. **e)** Representative confocal images of FHL2 localization and quantification of its nuclear-to-cytoplasmic ratio (n=3 gels for 36 to 46 cells) for MDA231 cells within 3D stiff and soft alginate hydrogels after 7 days of encapsulation (blue=DAPI, green=F-Actin, red=FHL2). Scale bar equals 10 μm, Mann-Whitney *U*-test ****p<0.0001. FHL2 fluorescence intensity (f.i.) per cell (n=3 gels for 59 to 151 cells) Mann-Whitney *U*-test ****p<0.0001. **f)** Quantification of FHL2 localization in 3D alginate stiff hydrogels after 7 days in the presence or absence of indicated inhibitors (n≥18 cells). Student's *t*-test with respect to control group (3D alginate stiff) ***p<0.001 and ****p<0.0001. **g)** Immunoblot showing FHL2 levels in MDA231 cells treated with two different anti-FHL2 siRNA oligos compared to untreated (control 1) or scramble (control 2) groups. GAPDH, glyceraldehyde-3-phosphate de-hydrogenase. **h)** Representative confocal images of p21 localization and quantification of its nuclear-to-cytoplasmic ratio (n=3 gels for 30 cells) for MDA231 normal and siRNA-FHL2 silenced cells within 3D stiff alginate hydrogels (blue=DAPI, green=F-Actin, red=p21). Scale bar equals 10 μm, Mann-Whitney *U*-test ****p<0.0001. Ki67 f.i. per cell (n= 74 to 260 cells), Mann-Whitney *U*-test ****p<0.0001. Datasets shown as box plots with median for 25th to 75th percentiles and whiskers for minimum and maximum. Violin plots show dashed lines for median and dotted lines for the two quartile lines. Error bars indicate mean and standard deviation.
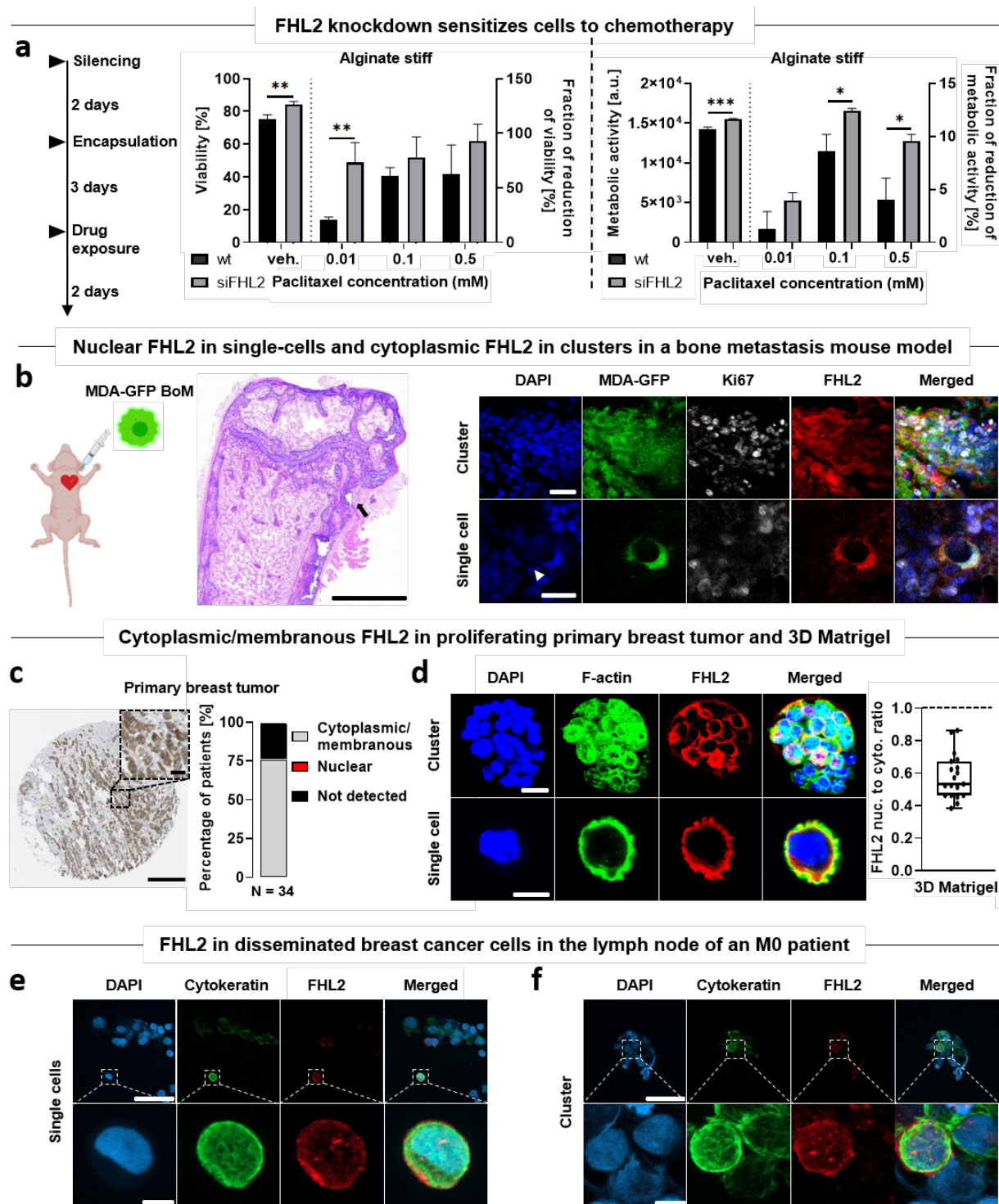
Fig. 5 FHL2 knockdown sensitizes cells to chemotherapy. FHL2 expression and localization in murine tissue of a breast cancer bone metastasis model, in human primary breast tumor and in early DCCs of an M0 patient. a) FHL2-silenced MDA231 cells were encapsulated for 3 days and exposed to Paclitaxel (0.01 to 0.5 mM) for 2 days, after which viability and metabolic activity (Presto Blue) measurements of normal and siRNA-FHL2 silenced cells within 3D alginate stiff were performed. Left y-axis corresponds to the overall viability and metabolic activity of vehicle (untreated groups). Right y-axis shows the fraction of reduction of viability and metabolic activity of drug treated groups with respect to the untreated group. Student's *t*-test (n=3 hydrogels) *p≤0.05,

p≤0.01, ***p≤0.001, ****p≤0.0001. Error bars indicate mean and standard deviation. **b) Intracardiac injection of GFP-tagged MDA-MB-231-1883 BoM cells in mice with representative Hematoxylin and Eosin (H&E) staining of the femur showing an osteolytic lesion (arrowhead). Representative confocal images of Ki67 (proliferation) and FHL2 localization of GFP-tagged MDA-MB-231-1883 BoM cells as single cells and clusters. Scale bars equal 1000 μm, 25 μm and 20 μm for H&E overview, cluster and single cell images, respectively. **c)** Representative immunohistochemical image of FHL2 localization in a female patient (50 years old) with breast ductal carcinoma. Fraction of FHL2 localization in 34 patients with primary breast ductal carcinoma. Data obtained from The Human Protein Atlas[58]. Scale bar equals 20 μm. **d)** Representative confocal images of FHL2 localization in spheroids and single MDA231 cells within 3D Matrigel after 7 days of encapsulation and quantification of its nuclear-to-cytoplasmic ratio (n=19 cells) (blue=DAPI, green=F-Actin, red=FHL2). Scale bar equals 20 μm for spheroid image and 10 μm for single cell image. **e, f)** Confocal images of cytokeratin (epithelial marker) and FHL2 (in single cells and within clusters) of human breast cancer cells disseminated in the sentinel lymph node of an M0 patient. Scale bars equal 50 μm and 5 μm for the wide and zoomed images, respectively.
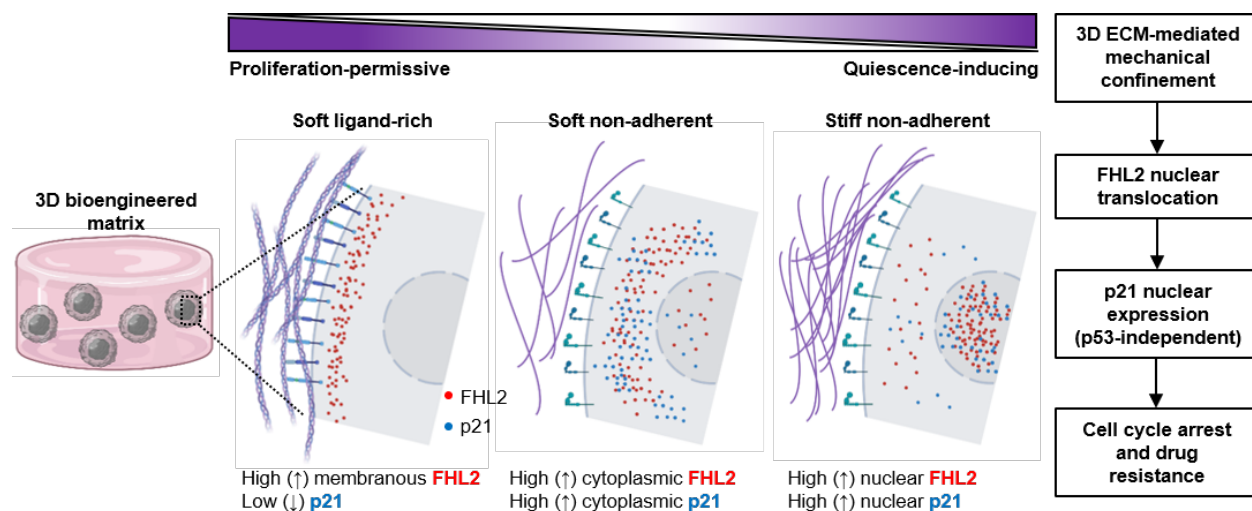
Fig. 6 Proposed stiffness-mediated FHL2 signaling mechanism in 3D bioengineered matrices inducing cancer cell quiescence and drug resistance. In proliferation-permissive, ligand-rich microenvironments such as basement membranes, stronger adhesion sites maintain FHL2 in the membranous regions. In low or non-adherent microenvironments, the increase in mechanical confinement (stiffness) results in FHL2 translocation to the nucleus, leading to high p21 nuclear expression and cell cycle arrest (graphical illustration created with BioRender.com).